INORGANIC CHEMISTRY FRONTIERS

RESEARCH ARTICLE

View Article Online
View Journal | View Issue

Cite this: *Inorg. Chem. Front.*, 2025, **12**, 8271

Dynamic room-temperature phosphorescence enabled by boronic acid group-mediated 2D perovskite heterojunctions for time-resolved multidimensional anti-counterfeiting and encryption

Peng Zhang, Xin Chen, Jing Li, Lei Fang and Xiangying Sun *

Dynamic room-temperature phosphorescence (RTP) materials with color-tunable afterglow characteristics hold great promise for advanced anti-counterfeiting and multidimensional encryption applications. In this work, we successfully synthesized a novel two-dimensional phenylammonium cadmium chloride perovskite (B-PACC) with enhanced RTP efficiency *via* boronic acid group-assisted crystallization. Furthermore, a precise doping strategy was employed to introduce Mn^{2+}, which assembled into Mn^{2+} pairs forming a Mn^{2+}-based inorganic layer. This layer, together with B-PACC, constructed a heterojunction structure with different interlayer spacings, enabling dynamic afterglow emission color modulation from red to blue. Moreover, tuning the Mn^{2+} concentration enables precise modulation of the energy transfer rates from the singlet and triplet states of the organic moieties to the Mn^{2+} layer, thereby allowing fine control over the dynamic RTP behavior. Benefiting from the minimal background interference and large chromaticity contrast associated with the red-to-blue phosphorescence transition, the system exhibited high visual detectability. Based on this dynamic afterglow behavior, we successfully developed time-resolved anti-counterfeiting patterns and constructed dynamic room-temperature phosphorescence-based four-dimensional (4D) codes, providing new insights into the design of dynamic RTP materials and highly secure encryption strategies.

Received 6th August 2025,
Accepted 30th August 2025

DOI: 10.1039/d5qi01664a

rsc.li/frontiers-inorganic

Introduction

Dynamic fluorescence-based multidimensional encoding has emerged as a promising strategy for advanced anti-counterfeiting and encryption, particularly due to the introduction of the time-dimension, which greatly improves both information capacity and security.[1–5] However, the transient emissions exhibited by these systems depend on continuous external stimuli and dynamic driving sources, inevitably introducing background interference and other uncontrollable factors. Therefore, it is of great significance to develop dynamic luminescent anti-counterfeiting and encryption systems capable of color variation under a single stimulus. Room-temperature phosphorescence (RTP) materials, which display persistent emission after the cessation of UV excitation, offer promising opportunities for constructing dynamic optical signal-based anti-counterfeiting systems under a single stimulus. Moreover, the absence of background interference from the stimulus endows them with extremely high visual sensitivity.[6–10] Nevertheless, most current RTP systems rely solely on intensity changes of a single emission color, limiting their encoding dimensions and capacities. Generally, two main strategies have been reported for achieving color-variable phosphorescence: the first involves multicomponent doping,[11,12] which is highly dependent on the compatibility among different phosphorescent materials and often suffers from issues such as chromatic cross-contamination and poor stability. The second strategy relies on the fine design and synthesis of single-component materials. Yet this approach requires complex control over excited-state dynamics, and only a few systems have been reported to date.[13,14] In addition, the construction of color-variable RTP systems still faces significant challenges: (1) the afterglow chromaticity must exhibit a substantial and easily visualized change; (2) the system should operate without requiring pretreatment or large instrumentation, making it applicable for on-site anti-counterfeiting and encryption. Therefore, there is an urgent need to develop

College of Materials Science and Engineering, Huaqiao University, Key Laboratory of Molecular Designing and Green Conversions (Fujian University), Xiamen 361021, China. E-mail: sunxy@hqu.edu.cn

single-component RTP materials with dynamic multicolor emission characteristics to realize multidimensional dynamic encoding under a single stimulus, meeting the application demands of high-security anti-counterfeiting and encryption systems.

Two-dimensional (2D) organic–inorganic metal halide perovskites have attracted considerable attention due to their outstanding luminescent properties. The inorganic halide layers can effectively suppress the nonradiative dissipation of triplet excitons generated by the organic layers, thereby enabling the realization of RTP properties. Meanwhile, the organic components offer highly tunable and flexible processability, allowing facile modulation of the luminescent characteristics.[15–19] Lv *et al.* introduced methoxy groups as substituents into the organic components of perovskites to modulate the frontier molecular orbitals, alter the triplet energy levels of the organic molecules, and achieve highly efficient and stable yellow-green RTP.[20] Additionally, doping strategies have been employed to flexibly tune the luminescent properties by introducing additional energy level structures. Zhou *et al.* designed and synthesized a 2D organic–inorganic metal halide hybrid (ABA_2CdCl_4), which exhibited efficient blue fluorescence and green RTP, upon doping with Mn^{2+} ions, tunable RTP colors between 270 and 333 K were achieved.[21] Furthermore, Zeng *et al.* developed a system based on the organic–inorganic hybrid metal halide $(Ph_3S)_2SnCl_6$, where Bi^{3+} and Sb^{3+} with lone-pair electrons were introduced to construct multiple energy transfer pathways, thus enabling fine modulation of the optical properties of self-trapped exciton (STE) fluorescence and organic phosphorescence.[22] However, although the RTP color itself can be precisely tuned, achieving dynamic color changes in RTP remains challenging. Therefore, precisely designing the organic components and dopant ions within 2D organic–inorganic metal halide perovskites to realize dynamic color-variable phosphorescence represents a significant challenge.

Boron-containing materials have attracted widespread attention in the field of luminescent materials in recent years due to the unique electron-deficient nature of boron atoms, which endows these systems with excellent fluorescence and RTP properties.[23–26] Typically, such materials can exhibit long-lived RTP without the need for additional regulation. For example, in 4-methoxyphenylboronic acid (PBA-MeO), intermolecular hydrogen bonding enhances molecular interactions, promoting dense packing and suppressing nonradiative processes, thereby achieving an RTP lifetime as long as 2.24 s.[27] Moreover, boronic acid groups can increase the rigidity of the system and stabilize triplet excitons and are thus frequently introduced into carbon dot systems as protective matrices to impart RTP characteristics.[28–30] For instance, Sun *et al.* constructed carbon dots with blue, green, and red RTP emissions by employing phenylboronic acid as the guest fluorophore and boronic acid-derived matrices as the host framework.[31] In contrast, within perovskite systems, boronic acid groups are more commonly used as ligands to passivate surface defects and enhance luminescence performance[32–34] yet reports on utilizing their structural features to achieve RTP are rare.

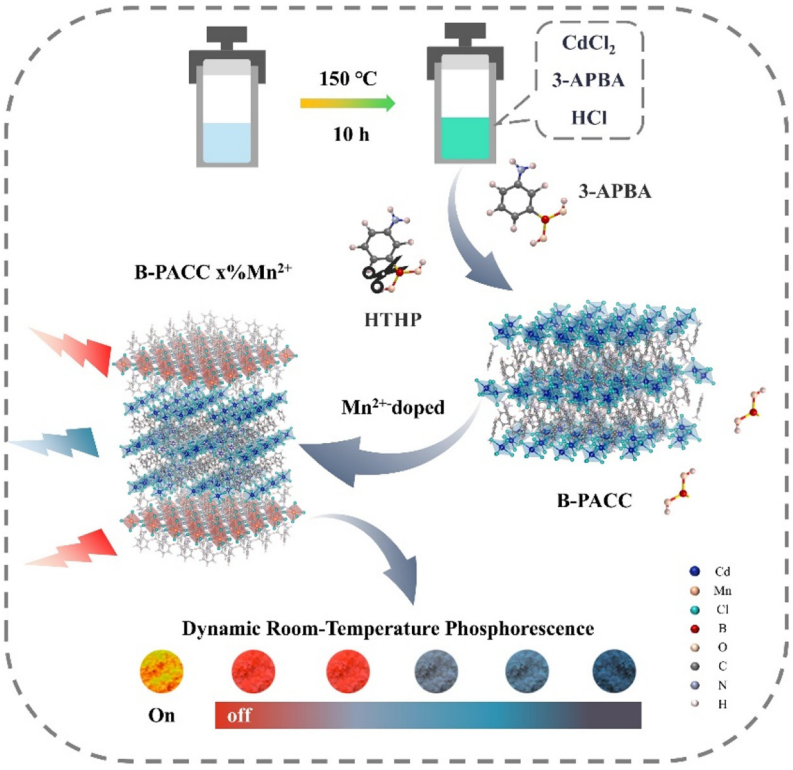

Scheme 1 Schematic illustration of the synthesis of Mn^{2+}-doped B-PACC with dynamic phosphorescence.

Accordingly, exploring boronic acid group-mediated strategies for the controlled synthesis of two-dimensional organic–inorganic metal halide perovskites to achieve more efficient RTP performance holds great research significance and promising application prospects.

In this work, we successfully regulated the crystallization process of 2D phenylammonium cadmium chloride perovskite (PACC) by introducing a sterically hindered boronic acid group during synthesis, leading to a reduction in the original organic layer spacing within the crystal. This boronic acid group-mediated PACC (B-PACC) possesses a more rigid crystal structure, thereby suppressing nonradiative transitions and extending the phosphorescence lifetime by approximately 17.1% (from 817 ms to 957 ms), ultimately resulting in more efficient RTP. Building on this, we further introduced Mn^{2+} doping to construct a heterojunction structure with an outermost layer composed of Mn^{2+}. This heterojunction facilitates efficient energy transfer from the singlet excited state of the organic component to both its triplet state and the Mn^{2+}-based inorganic layer, thereby enabling dynamic RTP color changes from red to blue (Scheme 1). Moreover, by tuning the Mn^{2+} concentration, the energy transfer rates from the singlet and triplet states of the organic moieties to the Mn^{2+} layer can be precisely modulated, allowing fine control over the dynamic RTP behavior. Owing to its minimal background interference and large chromaticity contrast associated with the red-to-blue phosphorescence transition, the system exhibits excellent visual detectability. We successfully applied this system to construct multidimensional dynamic encoding, achieving a room-temperature phosphorescence-based four-dimensional (4D) codes,[35] thus providing a new strategy for the development of dynamic RTP materials.

Results and discussion

We synthesized PACC and boronic acid group-mediated PACC (B-PACC) *via* a hydrothermal method. The crystal structure of B-PACC was determined by single-crystal X-ray diffraction (SC-XRD), as shown in Fig. 1a. Compared to the previously reported PACC structure,[36] B-PACC exhibits a more compact organic interlayer spacing and presents a typical orthorhombic system with a *Pbca* space group in a two-dimensional layered structure (Table S1). Fig. 1b shows the powder XRD patterns of samples synthesized by substituting aniline with varying amounts of *m*-aminophenylboronic acid. When *m*-aminophenylboronic acid is not used in the synthesis (0%), the diffraction pattern matches well with the simulated data from the PACC single crystal (1-Simulation). As its proportion in the synthesis increases, the crystal phase gradually transitions toward that of B-PACC, and when it reaches 100% in the synthesis, the diffraction pattern matches the B-PACC single-crystal simulation data (2-Simulation). Despite the substantial structural transformation, the luminescence properties remain relatively unchanged. As shown in Fig. 1c, with the increasing participation of boronic acid groups during synthesis, the internal

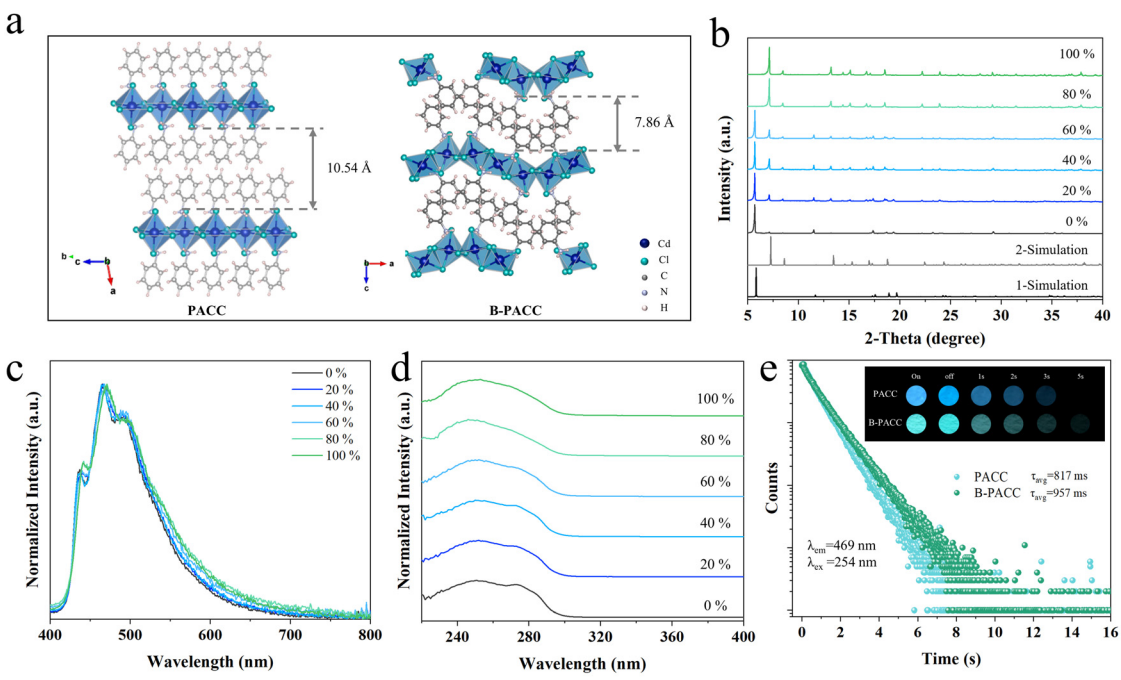

Fig. 1 (a) Schematic structures of PACC and B-PACC (*due to structural corrugation, the interlayer distance is defined as the vertical projection between inorganic slabs). (b) XRD patterns of samples synthesized with different substitution ratios of *m*-aminophenylboronic acid. (c) Fluorescence spectra of samples synthesized with different substitution ratios of *m*-aminophenylboronic acid under 254 nm excitation. (d) Excitation spectra at 469 nm of samples synthesized with different substitution ratios of *m*-aminophenylboronic acid. (e) Decay curves and room-temperature phosphorescence photographs of PACC and B-PACC.

interactions within the organic layers are strengthened, leading to a slight redshift and broadening of the fluorescence emission peaks, while the photoluminescence quantum yield (PLQY) remains nearly unchanged (Fig. S1a).[37] Consistently, the excitation spectra at 469 nm exhibit nearly identical profiles (Fig. 1d), suggesting that the emission centers remain consistent without any fundamental change. Furthermore, the reduced conjugation between benzene rings, caused by the decreased organic layer spacing, results in a decline in the excitation peak intensity at 270 nm.[38] Additionally, the enhanced rigidity of the overall crystal structure effectively suppresses nonradiative transitions, thereby extending the phosphorescence lifetime from 817 ms to 957 ms (Fig. 1e). To further investigate the emission mechanism, we conducted temperature-dependent Decay curves and phosphorescence measurements. The emission lifetimes of both PACC and B-PACC decreased with increasing temperature, and the phosphorescence intensity also diminished accordingly (Fig. S2a–d). These results exclude the possibility of thermally activated delayed fluorescence (TADF). We therefore speculate that the emission mechanism aligns with previously reported room-temperature phosphorescence (RTP).[36] Thus, the boronic acid group-mediated synthesis effectively enhances the crystal rigidity and prolongs the room-temperature phosphorescence lifetime, providing new insights for the design of more efficient RTP materials.

To further elucidate the electronic structures of B-PACC and PACC, we performed density functional theory (DFT) calculations. The calculated band gap of PACC is 3.634 eV, whereas the band gap of B-PACC synthesized *via* boronic acid group mediation increases to 3.718 eV (Fig. 2a and c). We attribute this band gap widening to the reduced interlayer spacing.[39] Additionally, due to the inherent band gap underestimation associated with the Perdew–Burke–Ernzerhof (PBE) functional,[40] the calculated band gap values are smaller than the experimental results (Fig. S3). Furthermore, the incorporation of boronic acid groups induces the formation of localized states near the conduction band edge. Compared to PACC, the projected density of states (Fig. 2d) for B-PACC exhibits an enhanced contribution from the organic components in the vicinity of the conduction band minimum (CBM). These states are likely induced by reduced interlayer spacing and enhanced interlayer electronic coupling, without significantly altering the overall band structure. In addition, compared to the original PACC system, B-PACC exhibits weaker hydrogen–hydrogen (H–H) interactions and enhanced carbon–hydrogen (C–H) interactions between organic units,[41] as shown in Fig. S4, which further verifies the formation of a more compact structure. This tighter packing effectively suppresses nonradiative relaxation during electronic transitions, leading to an extended phosphorescence lifetime.

To achieve multicolor dynamic RTP, we attempted to introduce Mn^{2+} into the B-PACC system, as their unique d-electron

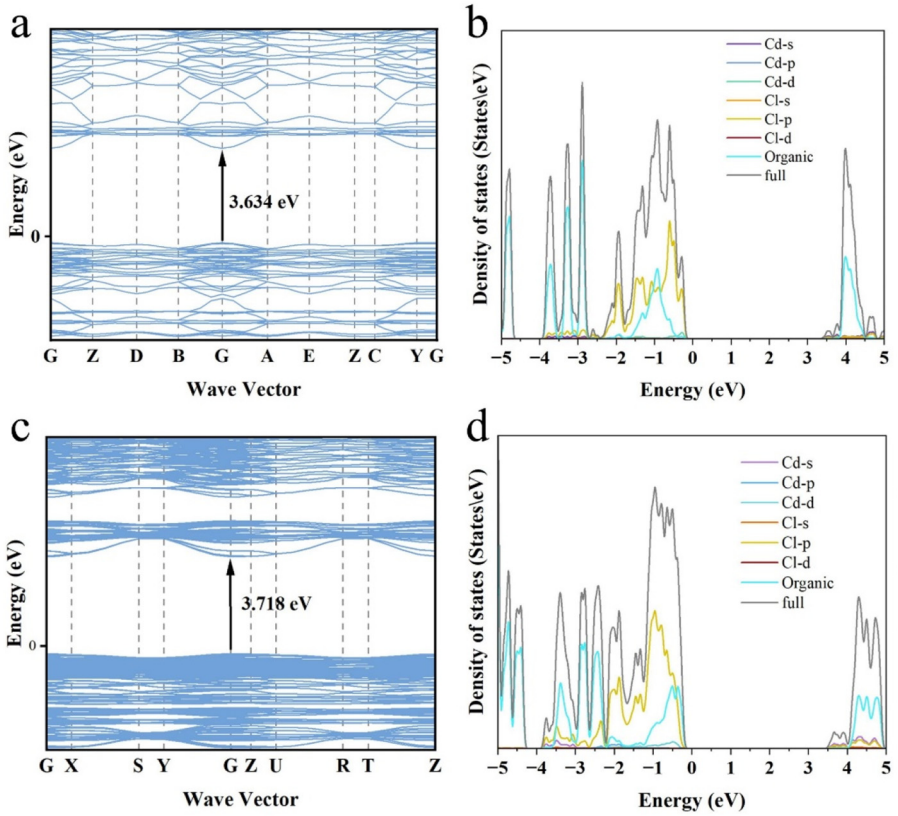

Fig. 2 Calculated electronic band structures of PACC (a) and B-PACC (c). Corresponding projected density of states of PACC (b) and B-PACC (d).

configuration typically gives rise to strong exchange interactions with the charge carriers of the host, thereby inducing energy transfer from the host to Mn^{2+} centers and resulting in tunable emission.[42,43] Due to the compact lattice structure of B-PACC, Mn^{2+} could not be uniformly incorporated into the crystal lattice but was preferentially inserted into the voids of the inorganic layers. It then gradually replaced Cd^{2+}, transforming the initially distorted inorganic layers of B-PACC into the planar structure characteristic of PACC. Inductively coupled plasma (ICP) measurements revealed that the actual amount of Mn^{2+} incorporated into the crystal was significantly lower than the nominal feeding ratio, further indicating the difficulty of Mn^{2+} incorporation into the lattice (Table S2). We speculate that Mn^{2+} preferentially localizes at the crystal surface instead of penetrating into the bulk, leading to the formation of a Mn^{2+}-rich layer with a PACC-like structure on the outer region of B-PACC (Fig. 3a). This hypothesis is supported by the XRD patterns of B-PACC samples doped with different concentrations of Mn^{2+}. As shown in Fig. 3b, B-PACC does not exhibit lattice shrinkage with increasing Mn^{2+} concentration but instead undergoes a structural transformation toward the PACC phase. In contrast, Mn^{2+} doping in PACC only leads to a slight shift of the XRD peaks toward higher angles, indicating simple lattice contraction without a phase change (Fig. S5). Based on a multiple lattice matching strategy, the lattice mismatch between the *a*-axis of the PACC crystal and the *c*-axis of the B-PACC crystal was calculated to be 3.48%. Given the identical chemical composition of PACC and B-PACC, this result provides a theoretical basis for the formation of a heterojunction between the two phases. The incorporation of Mn^{2+} successfully altered the optical properties of B-PACC. The corresponding photoluminescence (PL) spectra (Fig. 3c) reveal that as the Mn^{2+} concentration increases, the intrinsic emission peak of B-PACC gradually decreases, while a new emission

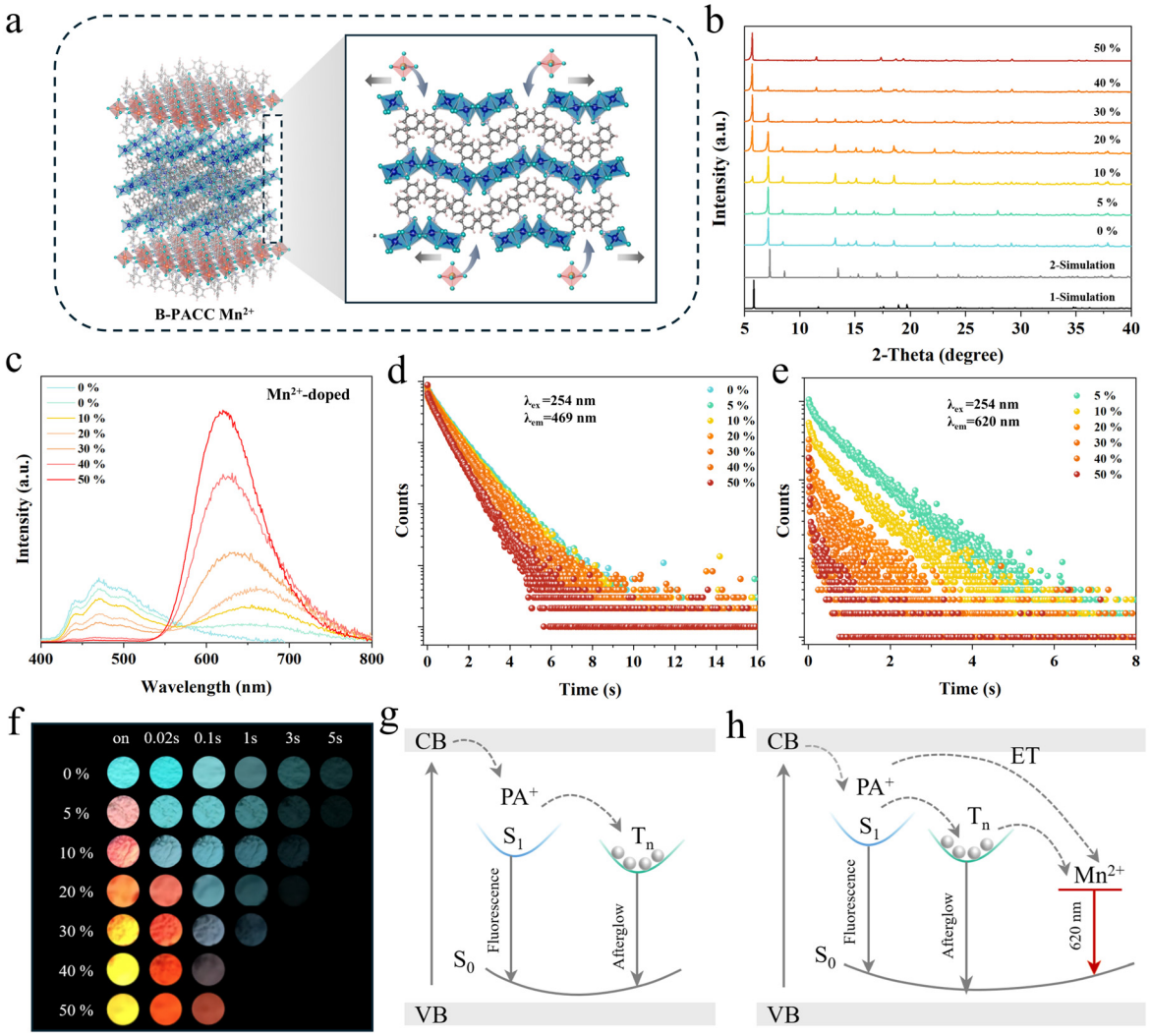

Fig. 3 (a) Schematic structure of Mn^{2+}-doped B-PACC. (b) XRD patterns, (c) photoluminescence spectra, (d) decay curves at 469 nm, (e) decay curves at 620 nm of samples with different Mn^{2+} doping concentrations. (f) Room-temperature phosphorescence photographs of samples synthesized with different Mn^{2+} doping concentrations. (g) Schematic illustration of the luminescence mechanism of B-PACC. (h) Schematic illustration of the luminescence mechanism of Mn^{2+}-doped B-PACC.

peak emerges around 650 nm, accompanied by a progressive increase in the PLQY (Fig. S1b). This new emission is attributed to the $^4T_1 \rightarrow {}^6A_1$ radiative transition of Mn^{2+} within the $[MnCl_6]^{4-}$ octahedra, indicating the existence of energy transfer from the organic components to the Mn^{2+} units. Moreover, at low Mn^{2+} concentrations, short Mn–Mn pairs are likely present within B-PACC. As the Mn^{2+} content increases, the recovery of a looser organic interlayer spacing, similar to that of PACC, increases the Mn–Mn distance, resulting in a weakened crystal field and a consequent blue shift of the 650 nm emission.[21] The excitation spectra at 469 nm (Fig. S6a) further support this observation: as Mn^{2+} incorporation leads to the recovery of a structure similar to PACC, the spatial spacing of the organic layers increases, restoring the conjugation between benzene rings and thereby enhancing the excitation peak intensity around 270 nm. Meanwhile, the excitation profiles around 620 nm remain essentially unchanged, indicating that the emission center remains consistent (Fig. S6b). Fig. 3d shows the average decay lifetimes of B-PACC:x%Mn^{2+} at 469 nm, which decrease with increasing Mn^{2+} concentration, primarily due to the energy transfer from the organic triplet states to the Mn^{2+} units. At 620 nm, as shown in Fig. 3e, the average lifetimes also decrease with further Mn^{2+} doping. We attribute this phenomenon to the formation of a large number of Mn^{2+} pairs at high Mn^{2+} concentrations. According to the diffusion-limited relaxation model proposed by Yokota and Tanimoto for dipole–dipole interactions, Mn^{2+} pairs decay much faster than isolated Mn^{2+} ions, leading to a shortened lifetime at high doping levels (Fig. S7).[42–44] Furthermore, electron paramagnetic resonance (EPR) spectra show that the signal intensity of B-PACC:50%Mn^{2+} is significantly lower than that of B-PACC:5%Mn^{2+} (Fig. S8), confirming the presence of strong Mn–Mn dipole–dipole interactions and the formation of more Mn^{2+} pairs at higher doping concentrations.

This Mn^{2+}-based inorganic layer, formed *via* Mn^{2+}–Mn^{2+} pairing, together with B-PACC, constitutes a heterojunction that successfully enables a dynamic RTP color transition from red to blue. As shown in Fig. 3f, the initial afterglow observed immediately after UV light cessation gradually shifts from blue-green to red with increasing Mn^{2+} concentration. Notably, at a doping level of 20%, an intriguing color-changing afterglow is observed. We speculate that the afterglow of PACC originates from the triplet state of the organic components (Fig. 3g). At lower Mn^{2+} concentrations, energy transfer occurs from both the singlet and triplet states of the organic moieties to the Mn^{2+} units, with the triplet-to-Mn^{2+} transfer being relatively slow. This results in a dynamic afterglow color shift from red to bluish-green (Fig. 3h). As the Mn^{2+} concentration increases, the Mn^{2+}-based outer layer becomes thicker, which enhances the rate of triplet-to-Mn^{2+} energy transfer and leads to a predominantly red afterglow. Time-resolved phosphorescence spectra for Mn^{2+} doping levels of 5%, 20%, and 50%

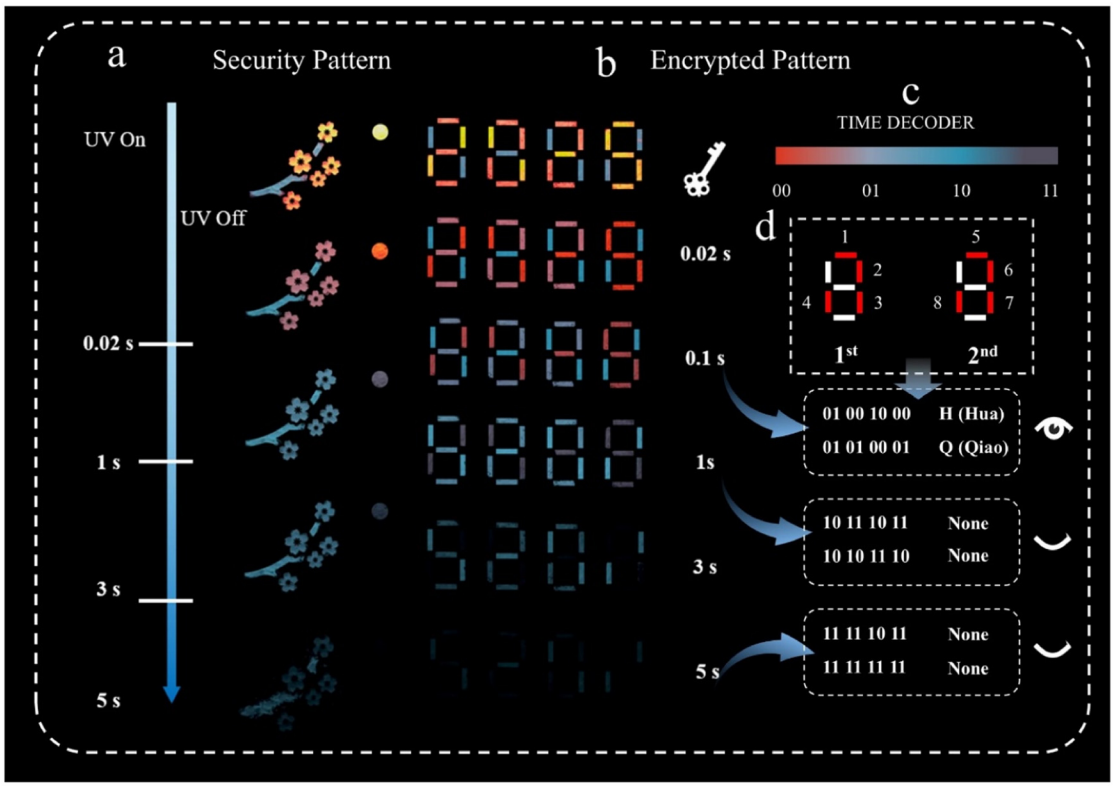

Fig. 4 (a) Dynamic room-temperature phosphorescence-based anti-counterfeiting pattern. (b and c) Dynamic room-temperature phosphorescence-based 4D codes and its corresponding decryption key. (d) Double-encryption regions of the dynamic room-temperature phosphorescence-based 4D codes.

were recorded (Fig. S9a–c), showing spectral evolution consistent with the visually observed afterglow colors (Fig. S9c–f). Among them, the samples with 5% and 20% Mn^{2+} doping exhibit significant afterglow color variation over time, making them suitable candidates for advanced anti-counterfeiting applications based on time-dependent afterglow color changes.

Based on the dynamic afterglow behavior of B-PACC:*x*% Mn^{2+}, we successfully developed time-resolved anti-counterfeiting patterns and dynamic room-temperature phosphorescence-based multidimensional encryption codes (4D codes). Specifically, as shown in Fig. 4a, we constructed an all-weather plum blossom pattern. Upon removal of the excitation light source, the pattern undergoes a transition from a full-color daytime image (red sun) to a distorted nighttime image (blue moon). Owing to the large color contrast during this transition, the process exhibits high visual detectability and requires only UV excitation for authentication (dynamic change during de-excitation). Additionally, the incorporation of the time variable significantly increases the difficulty of counterfeiting, rendering replication exponentially more challenging. Furthermore, we designed a dynamic room-temperature phosphorescence-based multidimensional encryption codes (4D codes), as illustrated in Fig. 4b. Details of the material composition are provided in Fig. S10. The code is composed of four numeral "8" patterns. After switching off the UV light, the first layer of information ("2025" and "520") can be retrieved at 0.02 s and 3 s, respectively. For the second layer of encryption, we assigned specific numerical values to different afterglow color ranges, as defined by the TIME DECODER shown in Fig. 4c. Each color region corresponds to two numerical codes. The true encrypted regions are embedded within the first two digits of the four "8" figures, where the red-highlighted areas represent the real coding zones. The decryption sequence is shown in Fig. 4d. Following this procedure, the digits in Fig. 4b acquire multidimensional meaning: at 0.1 s, decoding the first and second digits according to the decryption sequence yields "01001000" and "01010001", which correspond to the ASCII binary codes for the letters "H" and "Q", respectively. This correct answer only appears within 0.1 s after removing the excitation light, while decryption attempts at other times will yield false information. Such time-resolved multidimensional encoding thus provides a highly secure encryption strategy.

Conclusions

In this work, we successfully synthesized a novel two-dimensional phenylammonium cadmium chloride perovskite (B-PACC) with enhanced RTP efficiency through boronic acid group-assisted crystallization. Furthermore, by employing a precise doping strategy, Mn^{2+} ions were introduced to construct a novel heterojunction structure with different interlayer spacings, thereby achieving dynamic color-tunable phosphorescence from red to blue. Meanwhile, by tuning the Mn^{2+} concentration, the energy transfer rates from the singlet and triplet states of the organic moieties to the Mn^{2+} layer can be precisely modulated, allowing fine control over the dynamic RTP behavior. Moreover, the dynamic phosphorescence transition from red to blue, characterized by minimal background interference and a large chromaticity contrast, exhibited high visual detectability. We successfully applied this system to multidimensional dynamic encoding, constructing a room-temperature phosphorescence-based 4D codes, providing new insights into the design of dynamic RTP materials and advanced anti-counterfeiting and encryption strategies.

Author contributions

Peng Zhang: conceptualization, validation, formal analysis, investigation, data curation, methodology, and writing-original draft, review and editing. Xin Chen: review, supervision. Jing Li: review, Lei Fang: software. Xiangying Sun: funding acquisition, writing-review and editing, and supervision.

Conflicts of interest

There are no conflicts to declare.

Data availability

The data supporting this article have been included as part of the SI.

All data relevant to this study are available in the Supplementary Information, which contains methods, detailed experiments, and supplementary figures. See DOI: **https://doi.org/10.1039/d5qi01664a**.

CCDC 2430709 contains the supplementary crystallographic data for this paper.[45]

Acknowledgements

This work was supported by Foundation of Graphene Powder & Composite Research Centre of Fujian Province (No. 2017H2001) and Pilot Project of Fujian Province (No. 2021H0017). The authors also thank the Instrumental Analysis Center of Huaqiao University for analysis support.

References

1 X. Le, H. Shang, H. Yan, J. Zhang, W. Lu, M. Liu, L. Wang, G. Lu, Q. Xue and T. Chen, A Urease-Containing Fluorescent Hydrogel for Transient Information Storage, *Angew. Chem., Int. Ed.*, 2021, **60**(7), 3640–3646.

2 H.-Q. Zheng, Y. Yang, Z. Wang, D. Yang, G. Qian and Y. Cui, Photo-Stimuli-Responsive Dual-Emitting Luminescence of a Spiropyran-Encapsulating Metal–Organic Framework for

Dynamic Information Encryption, *Adv. Mater.*, 2023, **35**(26), 2300177.
3 Q. Wang, B. Lin, M. Chen, C. Zhao, H. Tian and D.-H. Qu, A dynamic assembly-induced emissive system for advanced information encryption with time-dependent security, *Nat. Commun.*, 2022, **13**(1), 4185.
4 P. Zhang and X. Sun, Advanced multicolor dynamic fluorescence anti-counterfeiting and encryption strategy based on light-induced reversible perovskite lattice distortion, *Chem. Eng. J.*, 2024, **498**, 155658.
5 P. Zhang, X. Chen, J. Li and X. Sun, Multi-Dimensional Dynamic Fluorescence of Perovskite Driven by Light/Heat for Anti-Counterfeiting and Encryption in Five-Dimensional Codes, *ACS Photonics*, 2025, **12**, 2720–2726.
6 H. Qiu, Y. Yan, H. Zhou, Z. Gao, S. Chen, C. Zhu and Z. Wang, Stimuli-responsive metal-free phosphorescent materials: From design and mechanisms to emerging applications, *Coord. Chem. Rev.*, 2025, **538**, 216734.
7 Y. Zhang, Q. Sun, L. Yue, Y. Wang, S. Cui, H. Zhang, S. Xue and W. Yang, Room Temperature Phosphorescent (RTP) Thermoplastic Elastomers with Dual and Variable RTP Emission, Photo-Patterning Memory Effect, and Dynamic Deformation RTP Response, *Adv. Sci.*, 2022, **9**(5), 2103402.
8 X. Yang, S. Wang, K. Sun, H. Liu, M. Ma, S.-T. Zhang and B. Yang, A Heavy-atom-free Molecular Motif Based on Symmetric Bird-like Structured Tetraphenylenes with Room-Temperature Phosphorescence (RTP) Afterglow over 8 s, *Angew. Chem., Int. Ed.*, 2023, **62**(34), e202306475.
9 K. Wang, L. Qu and C. Yang, Long-Lived Dynamic Room Temperature Phosphorescence from Carbon Dots Based Materials, *Small*, 2023, **19**(31), 2206429.
10 M. Gao, R. Wu, Y. Zhang, Y. Meng, M. Fang and J. Yang, New Molecular Photoswitch Based on the Conformational Transition of Phenothiazine Derivatives and Corresponding Triplet Emission Properties, *J. Am. Chem. Soc.*, 2025, **147**(3), 2653–2663.
11 X. Dou, T. Zhu, Z. Wang, W. Sun, Y. Lai, K. Sui, Y. Tan, Y. Zhang and W. Z. Yuan, Color-Tunable, Excitation-Dependent, and Time-Dependent Afterglows from Pure Organic Amorphous Polymers, *Adv. Mater.*, 2020, **32**(47), 2004768.
12 F. Lin, H. Wang, Y. Cao, R. Yu, G. Liang, H. Huang, Y. Mu, Z. Yang and Z. Chi, Stepwise Energy Transfer: Near-Infrared Persistent Luminescence from Doped Polymeric Systems, *Adv. Mater.*, 2022, **34**(15), 2108333.
13 Y.-J. Ma, Z. Qi, G. Xiao, X. Fang and D. Yan, Metal-Halide Coordination Polymers with Excitation Wavelength- and Time-Dependent Ultralong Room-Temperature Phosphorescence, *Inorg. Chem.*, 2022, **61**(41), 16477–16483.
14 T. Chen, Y.-J. Ma and D. Yan, Single-Component 0D Metal–Organic Halides with Color-Variable Long-Afterglow toward Multi-Level Information Security and White-Light LED, *Adv. Funct. Mater.*, 2023, **33**(18), 2214962.
15 H. Hu, D. Zhao, Y. Gao, X. Qiao, T. Salim, B. Chen, E. E. M. Chia, A. C. Grimsdale and Y. M. Lam, Harvesting Triplet Excitons in Lead-Halide Perovskites for Room-Temperature Phosphorescence, *Chem. Mater.*, 2019, **31**(7), 2597–2602.
16 B. Zhou and D. Yan, Simultaneous Long-Persistent Blue Luminescence and High Quantum Yield within 2D Organic–Metal Halide Perovskite Micro/Nanosheets, *Angew. Chem., Int. Ed.*, 2019, **58**(42), 15128–15135.
17 B. Zhou and D. Yan, Glassy inorganic-organic hybrid materials for photonic applications, *Matter*, 2024, **7**, 1950–1976.
18 Z. Qi, B. Zhoua and D. Yan, Recent advances in ultralong room-temperature phosphorescence materials based on metal–organic halides, *Mater. Chem. Front.*, 2023, **7**, 3475–3493.
19 Y. Wu, S. Lu, Q. Zhou, M.-G. Ju, X. C. Zeng and J. Wang, Two-Dimensional Perovskites with Tunable Room-Temperature Phosphorescence, *Adv. Funct. Mater.*, 2022, **32**(39), 2204579.
20 L. Ge, Y. Wang, X. Gao, M. Li, R. Zhang, S. Liu, Y. Yu, M. Li, L. Xu, Y. Tao, R. Chen and W. Lv, Stimulating Efficient and Stable Ultralong Phosphorescence of 2D Perovskites by Dual-Mode Triplet Exciton Stabilization, *Chem. Mater.*, 2022, **34**(19), 8917–8924.
21 Y. Peng, J. Ma, Y. Zhao, D. You, Y. Yao, Z. Deng, J. Liao, Y. Chang, W. Shen, M. Li, R. He and L. Zhou, Multilevel Stimulus-Responsive Room Temperature Phosphorescence Achieved by Efficient Energy Transfer from Triplet Excitons to Mn^{2+} Pairs in 2D Hybrid Metal Halide, *Adv. Funct. Mater.*, 2025, **35**(16), 2420311.
22 M. Ren, S. Zhang, J. Wu, Q. Hu, S. Cao, B. Zou, Z. Yin, W. W. Yu and R. Zeng, Engineered Energy Transfer in Room Temperature Phosphorescent Materials for Time-Resolved Dual-Mode Encryption, *Adv. Funct. Mater.*, 2025, **35**(16), 2420362.
23 W. He, X. Sun and X. Cao, Construction and Multifunctional Applications of Visible-Light-Excited Multicolor Long Afterglow Carbon Dots/Boron Oxide Composites, *ACS Sustainable Chem. Eng.*, 2021, **9**(12), 4477–4486.
24 Z. Wu, C. Herok, A. Friedrich, B. Engels, T. B. Marder and Z. M. Hudson, Impurities in Arylboronic Esters Induce Persistent Afterglow, *J. Am. Chem. Soc.*, 2024, **146**(46), 31507–31517.
25 D. Li, Z. Liu, M. Fang, J. Yang, B. Tang and Z. Li, Ultralong Room-Temperature Phosphorescence with Second-level Lifetime in Water Based on Cyclodextrin Supramolecular Assembly, *ACS Nano*, 2023, **17**(13), 12895–12902.
26 Q. Zhou, C. Yang and Y. Zhao, Dynamic organic room-temperature phosphorescent systems, *Chem*, 2023, **9**(9), 2446–2480.
27 Z. Chai, C. Wang, J. Wang, F. Liu, Y. Xie, Y.-Z. Zhang, J.-R. Li, Q. Li and Z. Li, Abnormal room temperature phosphorescence of purely organic boron-containing compounds: the relationship between the emissive behavior and the molecular packing, and the potential related applications, *Chem. Sci.*, 2017, **8**(12), 8336–8344.

28 Y. Bi, J. Yu, J. Xiao, K. Zhu, B. Wang, X. Xu and S. Lu, Visible Light Excited Time-Dependent Phosphorescence Color Tuning in Carbon Dots via Charge Transfer, *Angew. Chem., Int. Ed.*, 2025, e202506162, DOI: 10.1002/anie.202506162.
29 Z. Ran, H. Jia, Z. Zhong, H. Yang, Y. Zhu, Y. Li, J. Liu, X. Zhang, J. Zhuang, Y. Liu, B. Lei and C. Hu, Time-Dependent Room-Temperature Afterglow of Carbon Dots Constructed by Trap-Induced Multiemission Centers, *Nano Lett.*, 2025, **25**(17), 6993–7002.
30 F. Wang and X. Sun, Dual-Emission Afterglow of Carbon Dots Induced by an Inorganic Salt for Anticounterfeiting and Temperature Sensing, *Langmuir*, 2024, **40**(50), 26436–26442.
31 X. Wang, M. Ouyang, H. Wang and X. Sun, Preparation of Multicolor Room-Temperature Phosphorescence Carbon Dots by Changing the Conjugation Degree of Precursors for Information Encryption, *ACS Appl. Mater. Interfaces*, 2025, **17**(9), 14425–14432.
32 M. Yu, X. Mei, T. Qin, R. Zhuang, Y. Hua and X. Zhang, Modulating phase distribution and passivating surface defects of quasi-2D perovskites via potassium tetrafluoroborate for light-emitting diodes, *Chem. Eng. J.*, 2022, **450**, 138021.
33 T. Chen, X.-C. Ru, Z.-Y. Ma, L.-Z. Feng, K.-H. Song, J. Ge, B.-S. Zhu, J.-N. Yang and H.-B. Yao, Tetrafluoroborate-Passivated CsPbBrxCl3−x Nanocrystals for Spectrally Stable Pure Blue Perovskite Light-Emitting Diodes, *ACS Appl. Nano Mater.*, 2024, **7**(4), 4474–4480.
34 M.-S. Kim, P. Sadhukhan and J.-M. Myoung, High-Performance Blue Perovskite Films and Micro-Arrays for Light-Emitting Diodes with Ionic Liquid Interlayer, *Adv. Funct. Mater.*, 2024, **34**(1), 2309436.
35 Y. Zhou, L. Chen, P. Zhang, S. Cai, Z. Cai and F. Li, Light driven $CsPbI_3$ perovskite quantum dots core-shell transformation for Snapchat type anti-counterfeiting and encryption in 4D codes, *Chem. Eng. J.*, 2025, **508**, 160847.
36 S. Wang, S. Feng, R. Li, J. Jin, J. Wu, W. Zheng, Z. Xia, X. Chen, Q. Ling and Z. Lin, Multiexciton Generation from a 2D Organic–Inorganic Hybrid Perovskite with Nearly 200% Quantum Yield of Red Phosphorescence, *Adv. Mater.*, 2023, **35**(18), 2211992.
37 S. Tong, J. Dai, J. Sun, Y. Liu, X. Ma, Z. Liu, T. Ma, J. Tan, Z. Yao, S. Wang, H. Zheng, K. Wang, F. Hong, X. Yu, C. Gao and X. Gu, Fluorescence-based monitoring of the pressure-induced aggregation microenvironment evolution for an AIEgen under multiple excitation channels, *Nat. Commun.*, 2022, **13**(1), 5234.
38 W. Mueller-Markgraf and J. Troe, Thermal decomposition of ethylbenzene, styrene, and bromophenylethane: UV absorption study in shock waves, *J. Phys. Chem.*, 1988, **92**(17), 4914–4922.
39 Y. Lu, Y. Zhang, C.-Y. Yang, S. Revuelta, H. Qi, C. Huang, W. Jin, Z. Li, V. Vega-Mayoral, Y. Liu, X. Huang, D. Pohl, M. Položij, S. Zhou, E. Cánovas, T. Heine, S. Fabiano, X. Feng and R. Dong, Precise tuning of interlayer electronic coupling in layered conductive metal-organic frameworks, *Nat. Commun.*, 2022, **13**(1), 7240.
40 T. Chang, Q. Wei, R. Zeng, S. Cao, J. Zhao and B. Zou, Efficient Energy Transfer in Te4+-Doped Cs2ZrCl6 Vacancy-Ordered Perovskites and Ultrahigh Moisture Stability via A-Site Rb-Alloying Strategy, *J. Phys. Chem. Lett.*, 2021, **12**(7), 1829–1837.
41 P. R. Spackman, M. J. Turner, J. J. McKinnon, S. K. Wolff, D. J. Grimwood, D. Jayatilaka and M. A. Spackman, CrystalExplorer: a program for Hirshfeld surface analysis, visualization and quantitative analysis of molecular crystals, *J. Appl. Crystallogr.*, 2021, **54**(3), 1006–1011.
42 D. J. Robbins, E. E. Mendez, E. A. Giess and I. F. Chang, Pairing Effects in the Luminescence Spectrum of $Zn2SiO_4$: Mn, *J. Electrochem. Soc.*, 1984, **131**(1), 141.
43 C. Barthou, J. Benoit, P. Benalloul and A. Morell, Mn^{2+} Concentration Effect on the Optical Properties of Zn_2SiO_4: Mn Phosphors, *J. Electrochem. Soc.*, 1994, **141**(2), 524.
44 J. E. Lowther and J. A. Van Wyk, The effect of orbital variation of the spin-orbit interaction on the zero-field splitting of Mn^{2+}, *J. Magn. Reson.*, 1974, **13**(3), 328–335.
45 P. Zhang, X. Chen, J. Li, L. Fang and X. Sun, CCDC 2430709: Experimental Crystal Structure Determination, 2025, DOI: 10.5517/ccdc.csd.cc2mlbzk.